Probing optical anisotropy of nanometer-thin van der Waals microcrystals by near-field imaging

Debo Hu[1], Xiaoxia Yang[1], Chi Li[1], Ruina Liu[1], Ziheng Yao[2], Hai Hu[1], Stephanie N. Gilbert Corder[2], Jianing Chen[3], Zhipei Sun[4], Mengkun Liu[2], Qing Dai[1]

[1]Nanophotonics Research Division, CAS Center for Excellence in Nanoscience, National Center for Nanoscience and Technology, Beijing 100190, China.

[2]Department of Physics, Stony Brook University, Stony Brook, New York 11794, USA.

[3]Institute of Physics, Chinese Academy of Science, Beijing 100190, China.

[4]Department of Electronics and Nanoengineering, Aalto University, Tietotie 3, FI-02150 Espoo, Finland.

Correspondence should be addressed to Q.D. (E-mail: daiq@nanoctr.cn) and M.K.L. (E-mail: mengkun.liu@stonybrook.edu).

ABSTRACT: Most van der Waals crystals present highly anisotropic optical responses due to their strong in-plane covalent bonding and weak out-of-plane interactions. However, the determination of the polarization-dependent dielectric constants of van der Waals crystals remains a nontrivial task, since the size and dimension of the samples are often below or close to the diffraction limit of the probe light. In this work, we apply an optical nano-imaging technique to determine the anisotropic dielectric constants in representative van der Waals crystals. Through the study of both ordinary and extraordinary waveguide modes in real space, we are able to quantitatively determine the full dielectric tensors of nanometer-thin molybdenum disulfide and hexagonal boron nitride microcrystals, the most-promising van der Waals semiconductor and dielectric. Unlike traditional reflection based methods, our measurements are reliable below the length scale of the free-space wavelength and reveal a universal route for characterizing low dimensional crystals with high anisotropies.

Introduction

Symmetry breaking and intrinsic anisotropy are commonplace in low dimensional materials[1]. This is especially the case in two-dimensional (2D) van der Waals (vdW) crystals[2], where the strong in-plane covalent bonds and weak out-of-plane vdW forces naturally lead to highly anisotropic material properties. For example, the marked optical or electronic anisotropy has led to renowned investigations of hyperbolic dispersion in hexagonal boron nitride (h-BN)[3-7], linear dichroism in black phosphorus[8-10], spin-dependent relaxation in graphene[11-13], and valley polarization in molybdenum disulfide (MoS_2)[14,15]. By stacking 2D vdW crystals layer-by-layer into heterostructures (vdWHs)[16-19], a series of novel optoelectronic and photonic applications have been demonstrated as well, including light-emitting diodes[20,21], plasmonic waveguides[22-24], and photodetectors[25]. Although in their experimental infancy[26], these promising applications demand better identification of the anisotropic properties of various building blocks of vdWHs, to facilitate the rational design and optimization of vdWHs-based devices.

The optical anisotropy in vdW crystals, especially between the in-plane and out-of-plane directions, is challenging to measure. It is more so in the case of mechanically exfoliated crystals, which are known to possess superior crystalline qualities. The typical size of the exfoliated vdW crystals can be of the order of a few microns, which prohibits most of the common diffraction limited characterization techniques such as edge reflection (requiring large sample thickness and surface area, ~mm^3-scale volume at least; in addition, fine polished cross-sectional surface is required to measure the out-of-plane dielectric constant)[27] and ellipsometry (requiring oblique incident angles and large sample area, ~100×55 μm^2 at least)[28]. Therefore, it is a nontrivial task to obtain the intrinsic polarization-dependent optical properties of high-quality vdW crystals. A novel

method is highly desired for evaluating and quantifying the optical anisotropy of nanometer-thin vdW microcrystals.

In this work, we elaborate on a method for characterizing the optical anisotropy of nanometer-thin vdW microcrystals. Using a scattering-type scanning near-field optical microscope (s-SNOM), the full dielectric tensor of vdW nanoflakes can be quantitatively extracted from real-space mapping of the ordinary and extraordinary waveguide modes. With this method, we report the first measurement of the dielectric tensor of MoS_2 microcrystals (In-plane/Out-of-plane permittivity is 20.25/9.61) in the near-infrared region (wavelength λ =1530 nm). By extending the working wavelength to the visible region (wavelength λ =632.8 nm), the optical anisotropy of h-BN can also be characterized (In-plane/Out-of-plane permittivity is 5.33/2.99) and compared to the previous reported results. This work breaks the experimental bottleneck necessitating large-size samples in order to characterize the polarization-dependent optical properties of low-dimensional vdW crystals.

Results

Theoretical foundation for the method. Since MoS_2 is a uniaxial vdW crystal with its optic axis *c* perpendicular to the basal plane (Supplementary Fig. 1), its relative dielectric tensor can be written as

$$\|\varepsilon\| = \begin{bmatrix} \varepsilon_{\perp} & 0 & 0 \\ 0 & \varepsilon_{\perp} & 0 \\ 0 & 0 & \varepsilon_{\mathrm{P}} \end{bmatrix}, \quad (1)$$

where $\varepsilon_{\perp}$ is the in-plane relative dielectric constant (perpendicular to the optic axis), and ε_{P} is the out-of-plane relative dielectric constant (parallel to the optic axis). In analogy with the ordinary and extraordinary rays in the bulk anisotropic crystals[29], it can be proved theoretically

(Supplementary Note 1) that there are ordinary and extraordinary waveguide modes propagating in the anisotropic MoS_2 nanoflakes. The eigenequations of the waveguide modes can be written as

$$\sqrt{\varepsilon_{\perp}k_0^2-\beta_{\mathrm{o}}^2}\,d=\tan^{-1}\left(\frac{\sqrt{\beta_{\mathrm{o}}^2-k_0^2\varepsilon_1}}{\sqrt{\varepsilon_{\perp}k_0^2-\beta_{\mathrm{o}}^2}}\right)+\tan^{-1}\left(\frac{\sqrt{\beta_{\mathrm{o}}^2-k_0^2\varepsilon_2}}{\sqrt{\varepsilon_{\perp}k_0^2-\beta_{\mathrm{o}}^2}}\right)+m\pi \tag{2}$$

and

$$\sqrt{\frac{\varepsilon_{\perp}}{\varepsilon_{\mathrm{P}}}}\sqrt{\varepsilon_{\mathrm{P}}k_0^2-\beta_{\mathrm{e}}^2}\,d=\tan^{-1}\left(\frac{\sqrt{\beta_{\mathrm{e}}^2-k_0^2\varepsilon_1}\,\varepsilon_{\perp}}{\sqrt{\frac{\varepsilon_{\perp}}{\varepsilon_{\mathrm{P}}}}\sqrt{\varepsilon_{\mathrm{P}}k_0^2-\beta_{\mathrm{e}}^2}\,\varepsilon_1}\right)+\tan^{-1}\left(\frac{\sqrt{\beta_{\mathrm{e}}^2-k_0^2\varepsilon_2}\,\varepsilon_{\perp}}{\sqrt{\frac{\varepsilon_{\perp}}{\varepsilon_{\mathrm{P}}}}\sqrt{\varepsilon_{\mathrm{P}}k_0^2-\beta_{\mathrm{e}}^2}\,\varepsilon_2}\right)+n\pi\,, \tag{3}$$

respectively (Supplementary Note 2). In equation 2 and 3, $k_0=2\pi/\lambda$ is the free-space wavevector; β_{o} and β_{e} are the in-plane wavevectors for ordinary and extraordinary waveguide modes, respectively; d is the thickness of MoS_2 nanoflakes; ε_1 and ε_2 are relative dielectric constants of the isotropic superstrate and substrate, respectively; m and n are the order numbers (non-negative integers) of ordinary and extraordinary waveguide modes, respectively. According to the two transcendental equations above, the ordinary waveguide modes are transverse electric (TE) polarized, and their in-plane wavevectors are only related to the in-plane relative dielectric constant of MoS_2; the extraordinary waveguide modes are transverse magnetic (TM) polarized, and their in-plane wavevectors are related to the in-plane and out-of-plane relative dielectric constants. Therefore, once the in-plane wavevectors of both the ordinary and extraordinary waveguide modes are determined for at least two MoS_2 nanoflakes with different thicknesses, the in/out-of-plane relative dielectric constants can be found explicitly utilizing equation 2 and 3.

Experimental verification of the imaging principle. In this work, the atomic force microscope (AFM) based s-SNOM with nanoscale spatial resolution is employed to simultaneously acquire

both the sample thickness and the in-plane wavevectors required by equation 2 and 3. The experimental setup and imaging principle are illustrated in Figure 1a and 1b.

As shown in Figure 1a, the MoS_2 nanoflakes on SiO_2/Si substrates are preferentially oriented under the s-SNOM such that the sharp edges of the nanoflakes (coincident with the Y axis) are parallel to the AFM cantilever. The AFM cantilever can be used as a reference to infer geometric factors: the angle between the illumination wavevector k_0 and its projection k_{xy} in the X-Y plane (coincident with the sample surface) is α =38°; the angle between k_{xy} and the investigated sample edge is β =60° (indicated in the top view). The near-infrared laser at λ =1530 nm with 3 μm spot size was focused onto the apex of the s-SNOM tip to excite both ordinary and extraordinary waveguide modes in the MoS_2 nanoflakes. These modes can propagate in the MoS_2 nanoflakes as cylindrical waves, get scattered into the far-field as free-space light at the sample edges or, in principle, back-reflected. Because their in-plane wavevectors are far smaller than those of the graphene surface plasmon polaritons (SPPs)[30,31] and h-BN surface phonon polaritons (SPhPs)[32], back-reflection of the waveguide modes at the sample edges is fairly insufficient compared to those previously studied cases[33,34]. Therefore, the acquired s-SNOM images are dominated by the interference fringe patterns formed between the tip scattered light and the edge scattered light as illustrated in Figure 1b, implying significant dependence on the sample edge orientation. This makes the imaging principle of the waveguide modes different from those for graphene SPPs and h-BN SPhPs, where the resulting s-SNOM images are standing wave patterns formed by the incident and reflected surface waves, exhibiting no dependence on the sample edge orientation. Due to the asymmetry introduced by the incident angle, the optical path difference (OPD) between the tip scattered light $E_s(O')$ and the left side edge scattered light $E_s(O'')$ is different from that

between $E_s(O')$ and the right side edge scattered light $E_s(O)$ (Note that the edge scattered light in the vicinity of O and O" has the major contribution to the near-field contrast since the net scattering from all the other points will be diminished due to the in-plane symmetry and destructive interference). Therefore the fringe spacing at the left half of the resulting s-SNOM image Λ_L is different from Λ_R at the right half. Based on the simple geometry in Figure 1a, the genuine in-plane wavevectors of ordinary and extraordinary waveguide modes of MoS_2 nanoflakes, $\beta_{o,e}$, can be extracted either from the left side apparent wavevector $k_L = 2\pi / \Lambda_L$ as

$$\beta_{o,e} = \frac{2\pi}{\Lambda_L} + k_0 \cos\alpha \sin\beta , \tag{4}$$

or from the right side apparent wavevector $k_R = 2\pi / \Lambda_R$ as

$$\beta_{o,e} = \frac{2\pi}{\Lambda_R} - k_0 \cos\alpha \sin\beta . \tag{5}$$

We first demonstrate the validity of the above imaging principle experimentally with an 81-nm-thick MoS_2 sample placed in the same orientation as in Figure 1a, i.e. β=60° (see Supplementary Fig. 2 for AFM images and height profiles). The real-space s-SNOM image together with the corresponding fringe profile is shown in the upper panel of Figure 1c. As expected, the fringe spacings are different at the opposite edges: the spacing at the left edge is 747 nm (corresponding to an apparent in-plane wavevector $k_L = 2.048k_0$), while at the right it is 448 nm ($k_R = 3.415k_0$). The wavevector information can be represented more clearly in the momentum space as shown in the upper panel of Figure 1d by imposing a Fourier transform (FT) on the real-space fringe profile (see Supplementary Fig. 3 for detailed data processing method). The frequency peaks at the local maxima correspond to the apparent in-plane wavevectors k_L and k_R derived from the spatial

domain, and their frequency difference coincides with the theoretical value $1.365k_0$ given by equation 4 and 5. When β is reduced to 35° via sample rotation, a smaller (larger) fringe spacing at the left (right) edge is observed (lower panel of Figure 1c) and the frequency difference between k_L and k_R is decreased (lower panel of Figure 1d). More importantly, experiments at different β's produce the same in-plane wavevector $2.735k_0$ for the waveguide mode in the same sample, validating the rigorous parameter extraction procedure. Therefore, we have established a self-consistent method to measure the in-plane wavevectors of waveguide modes propagating in the nanometer-thin vdW microcrystals using s-SNOM.

Extraction of the dielectric tensor from real-space images. Since the MoS_2 nanoflake in Figure 1c is relatively thin, it supports only one waveguide mode – the fundamental ($m = 0$) ordinary mode, i.e. the TE_0 mode. For thicker MoS_2 flakes, two and more distinct modes can be observed. For example, in a 103-nm-thick MoS_2 flake, a fundamental extraordinary mode (TM_0 mode) and a trivial low-frequency air mode are evident in addition to the TE_0 mode (Figure 2). The wavevector of the trivial air mode equals $k_0(1+\cos\alpha\sin\beta)$, and does not shift with the increasing sample thickness. The apparent wavevectors of the TM_0 and TE_0 modes are thickness-dependent, which shift towards higher frequencies and eventually separate themselves from the air modes as the sample thickness is increased above ~150 nm, as shown in Figure 2b.

The TE_0 mode provides an in-plane wavevector $k_R - k_0\cos\alpha\sin\beta$. By substituting the two sets of experimental data (d_1=81 nm, $\beta_{o1} = 2.735k_0$; d_2=103 nm, $\beta_{o2} = 3.06k_0$) into equation 2, we get the in-plane dielectric constant $\varepsilon_\perp = 20.25$ and the TE mode order number $m = 0$. Similarly, the in-plane wavevectors of the TM_0 modes are determined to be $1.733k_0$ and $2.007k_0$ for the

170-nm-thick and 198-nm-thick samples, respectively. By substituting these two sets of data (d_3 =170 nm, $\beta_{e1} = 1.733k_0$; d_4 =198 nm, $\beta_{e2} = 2.007k_0$) into equation 3, one can get the out-of-plane dielectric constant $\varepsilon_P = 9.61$ and the TM mode order number $n = 0$. Therefore, the relative dielectric tensor of MoS_2 governing its optical anisotropy at the important optical communication wavelength 1530 nm can be quantitatively determined to be

$$\|\varepsilon\| = \begin{bmatrix} 20.25 & 0 & 0 \\ 0 & 20.25 & 0 \\ 0 & 0 & 9.61 \end{bmatrix}, \quad (6)$$

which clearly demonstrates that the MoS_2 nanoflakes are indeed negative crystals since the extraordinary index of refraction ($n_e = \sqrt{\varepsilon_P} = 3.1$) is less than the ordinary one ($n_o = \sqrt{\varepsilon_\perp} = 4.5$). Note that we choose to calculate the out-of-plane (in-plane) dielectric constant using the thicker (thinner) samples because the corresponding wavevectors are the most prominent with those thicknesses, yielding a more accurate parameter extraction. The experimentally obtained dielectric tensor of MoS_2 is in very good agreement with theoretical values by first principle calculations ($\varepsilon_\perp = 16.8$, $\varepsilon_P = 9.0$, note that these are stationary values calculated at long wavelength limit; at 1530 nm, the values are indeed expected to be larger)[35,36].

Discussion

As demonstrated above, to disentangle the in-plane and the out-of-plane dielectric constants and quantify the full dielectric tensor of the investigated vdW microcrystals, one has to image both TE polarized ordinary and TM polarized extraordinary waveguide modes. The aperture-type SNOM (a-SNOM) has been widely used in the waveguide mode imaging as demonstrated in the previous works[37,38]. Compared to a-SNOM, we suggest using s-SNOM to study the anisotropy of low-

dimensional vdW microcrystals is preferred due to its wavelength-independent high spatial resolution (~10 nm) and ultra-broadband compatibility. However, imaging the TE modes with s-SNOM is not a routine work since it has been long believed that s-SNOM can only effectively excite and pick up the TM polarized near-field signals due to the elongated tip geometry perpendicular to the sample surface. Nevertheless, we managed to image the TE polarized waveguide modes for the first time. The imaging capability of the s-SNOM for TE polarized modes remained undiscovered in the past mostly because the s-SNOM has been applied mainly in the mid-infrared region where the TM-polarized field dominates the near-field scattering signal[39]. In addition, the surface or waveguide modes such as graphene SPPs[30,31] and h-BN SPhPs[32] investigated in the previous s-SNOM experiments are exclusively TM polarized. The s-SNOM imaging of TE polarized waveguide modes in this work can be attributed to the reduced working wavelength in the visible and near-infrared frequency ranges, where the tip geometry perpendicular to the sample surface is less important for determining the scattered near-field signal (in contrast, a spheroidal finite-dipole description is required in the mid-infrared as a result of the long working wavelength)[40].

We calculated the thickness dispersions of the fundamental ordinary (TE_0) and extraordinary (TM_0) waveguide modes in the air-MoS_2-SiO_2 three-layer waveguide using equations 2 and 3 by assuming the superstrate air and the substrate SiO_2 are both semi-infinite and taking their isotropic dielectric constants to be 1.00 and 2.15 at the 1530 nm wavelength[41], respectively. The calculation results shown in Figure 3a agree well with the in-plane wavevectors of the fundamental ordinary waveguide mode (TE_0) in the 170-nm-thick and 198-nm-thick MoS_2 samples (extracted from Figure 2b). The slight deviation between the experimental and the simulated wavevector values for the 103-nm-thick sample is caused by the uncertainty in reading the position of the TM_0 peak

in Figure 2b due to the air-TM_0 modes overlapping mentioned above. Figure 3a indicates the cut-off thicknesses for TE_0 and TM_0 modes in the air-MoS_2-SiO_2 asymmetrical waveguide are about 15 nm and 85 nm, respectively. Waveguides with MoS_2 thickness larger than 85 nm can support both TE_0 and TM_0 modes; waveguides with MoS_2 thickness in the interval between 15 and 85 nm can only support the TE_0 mode; and when the MoS_2 layer is thinner than 15 nm it cannot support any mode. The theoretically predicted cut-off of the fundamental extraordinary waveguide mode below the thickness of 85 nm explains the observed single mode behavior of the 81-nm-thick sample shown in Figure 2b. Thus, all the experimental results are in good agreement with each other in the framework of anisotropic waveguide theory.

The cut-off behaviors of the ordinary and extraordinary modes in asymmetrical waveguides (superstrate and substrate are of different dielectric constants, $\varepsilon_1 \neq \varepsilon_2$) seemingly set a lower limit for the sample thickness we can investigate (Figure 3a). However, the theoretical calculations demonstrate that the cut-off thicknesses of the fundamental modes decrease with the increasing degree of symmetry of the MoS_2 waveguide (Supplementary Fig. 4); when the waveguide is perfectly symmetrical ($\varepsilon_1 = \varepsilon_2$) the fundamental modes do not cut off. Thus, by suspending the samples to eliminate the asymmetry, we can reduce this cut-off thickness for the fundamental waveguide modes. As shown in Figure 3b, the in-plane wavevectors of both the ordinary and extraordinary fundamental modes approach the free-space wavevector asymptotically with the decreasing sample thickness, thus probing the optical anisotropies of few-layer or even monolayer samples utilizing our method is possible if the unwanted air mode can be suppressed. This is indeed probable since the air mode becomes weaker with the decreasing sample thickness as shown in Figure 2b.

The contrast of the near-field images also has strong sample thickness dependence and is expected to fade out completely for samples much thicker than 200 nm (Figure 2a and Figure 3c). With increasing MoS_2 sample thickness, the normalized electric field profile (Supplementary Note 3) of the fundamental ordinary mode shifts into the substrate, coupling much less with the s-SNOM tip-induced hot spot at the sample surface (see inset of Figure 3c). This results in a decreased excitation efficiency of the waveguide mode and subsequent loss of interference visibility (i.e. image contrast). This fringe visibility of the lower order modes sets an upper limit for the sample thickness. For high order modes, however, the evanescent fields extend much further out the sample surface, leading to higher excitation efficiencies and therefore enhanced interference visibilities with thicker samples (Supplementary Fig. 5 and Fig. 6). Generally speaking, the number of waveguide modes increases with the thickness of the MoS_2 layer. For a waveguide with a 1000-nm-thick MoS_2 layer, there are five TE modes (m=0~4) and five TM modes (n=0~4) (Supplementary Fig. 7) available for near-field imaging. Therefore, the sample thickness in our method is only limited by the maximum height measurement range of the AFM embedded in our s-SNOM (~1000 nm).

The last feature that cannot be overlooked in our experimental results is the unbalanced mode strength ratio between the fundamental ordinary and extraordinary modes in the momentum-space spectra as shown in Figure 2b. To explain this phenomenon, we have to take the finite SiO_2 substrate thickness (typical value 300 nm) into consideration because the waveguide modes tend to leak out through the SiO_2 layer into the high refractive index Si layer below. As shown in Figure 3d, the extraordinary mode (blue curve) in the 170-nm-thick MoS_2 sample retains a stronger electric field at the virtual SiO_2/Si interface than the ordinary mode (black curve), and hence experiences much higher dissipation during propagation[42] which manifests as a low and broad

peak in the momentum space. Therefore, we can reduce the transmission loss of the extraordinary mode by increasing the thickness of the SiO_2 layer, which narrows its corresponding peak in the momentum space. This allows a more accurate determination of the out-of-plane dielectric constant by reducing the uncertainty in the peak position fitting procedure.

The application of our method can also be validated for other vdW crystals as long as their transparent or low-loss frequency windows are known. For example, optical anisotropy of h-BN at the wavelength 632.8 nm has been investigated. Two h-BN samples with the thicknesses 75 nm and 230 nm are analyzed as shown in Figure 4a and 4b, respectively (see also Supplementary Fig. 8 and Fig. 9). As shown in Figure 4a, Fourier analysis of the left-half of the fringe profile produces an air mode located at $0.335k_0$, indicating a different incident angle $\alpha = 39.8°$ for the visible laser from the one for the near-infrared laser ($38°$), this is quite reasonable since the visible and the near-infrared lasers cannot be in perfect alignment in the s-SNOM. Analysis of the other two peaks (TE_0) in Figure 4a using equation 4 and 5 produces the same in-plane wavevector ($1.68k_0$) for the fundamental ordinary mode propagating in the 75-nm-thick h-BN sample; taking the small incline angles of the sample edges shown in Supplementary Fig. 9 into consideration, we can derive the in-plane wavevectors from Figure 4b for the fundamental ordinary and extraordinary waveguide modes propagating in the 230-nm-thick h-BN sample ($2.113k_0$ and $1.556k_0$, respectively) as well. Thus the in-plane and out-plane relative dielectric constants of h-BN at 632.8 nm are determined to be 5.33 and 2.99, respectively, corresponding to an ordinary refractive index n_o=2.31 and an extraordinary refractive index n_e =1.73, respectively. The experimentally obtained refractive indices are slightly larger than those previously reported in artificially synthesized BN sample ($n_o = 2.13,\ n_e = 1.65$)[43], probably because the polycrystalline and porous structure of the artificial

BN sample used in the previous work tends to lower the refractive indices[44] as compared with the intrinsic ones of the mechanically cleaved monocrystals used in this work.

The investigated MoS_2 and h-BN samples in this work are uniaxial crystals. Nevertheless, this method can be applied to the much more complicated biaxial vdW crystals. To this end, one has to determine the two in-plane principal axes for the biaxial crystals by other techniques like Raman spectroscopy[45] and second-harmonic generation (SHG)[46]. Waveguide mode imaging can be performed at the two sharp edges perpendicular to the two principal axes, naturally formed while crystal growth or machined using microfabrication techniques. The in-plane dielectric constant associated with each principal axis can be extracted following the same procedure used in the uniaxial vdW crystals characterization.

When properly mapped and characterized, the waveguide modes propagating in 2D materials can be a convenient way to determine the in-plane and out-of-plane dielectric constants. By employing near-field scanning methods, our work overcomes the challenge of measuring small-size samples of vdW crystals and provides two specific yet universally relatable examples in MoS_2 and h-BN. The variations of the current method can lead to practical solutions for probing samples of in-plane anisotropy and few-layer or monolayer thickness. Further investigations will allow us to address important material properties at the nanoscale, such as the local dielectric properties around crystalline defects or the sub-wavelength polaritonic interactions in anisotropic nano-devices.

Methods

Sample Preparation

Silicon wafers with 300-nm-thick SiO_2 top layer were used as substrates for all the samples. The MoS_2 and h-BN microcrystals of various thicknesses were exfoliated from bulk samples.

Near-field Optical Measurement

The nano-imaging experiments described in the main text were performed using a commercial s-SNOM (www.neaspec.com). The s-SNOM is based on a tapping-mode AFM illuminated by monochromatic lasers of the wavelength 1530 nm or 632.8 nm (www.toptica.com). The near-field images were registered by pseudo-heterodyne interferometric detection module with tip tapping frequency around 270 kHz, the tip tapping amplitudes are 50 nm for the 1530-nm-wavelength experiments and 30 nm for the 632.8-nm-wavelength experiments. By demodulating the optical signal at the third order harmonic of the tip tapping frequency, the noise from the background and stray light can be greatly suppressed. The spot sizes of the visible (632.8 nm) and near-infrared (1530 nm) beam at the focus under the AFM tip are approximately 1.5 μm and 3 μm, respectively, which are in favor of the tip-launching and edge-scattering detection scheme proposed in this research. Although there are certain areas near the edges where edge-launched waveguide modes exist, we can remove this edge effect in the data processing by windowing the real-space fringe profiles in the Fourier transform.

Data Availability

The data that support the findings of this study are available from the corresponding authors upon reasonable request.

References

1 Li, Q. *et al*. *Anisotropic Nanomaterials: Preparation, Properties, and Applications*; Springer: 2015.
2 Novoselov, K. S. *et al*. Two-dimensional Atomic Crystals. *Proc. Natl. Acad. Sci. U.S.A.* **102**, 10451-10453 (2005).
3 Caldwell, J. D. *et al*. Sub-diffractional Volume-confined Polaritons in the Natural Hyperbolic Material Hexagonal Boron Nitride. *Nat. Commun.* **5**, 5221 doi:10.1038/ncomms6221 (2014).
4 Dai, S. *et al*. Subdiffractional Focusing and Guiding of Polaritonic Rays in a Natural Hyperbolic Material. *Nat. Commun.* **6**, 6963 doi:10.1038/ncomms7963 (2015).
5 Li, P. *et al*. Hyperbolic Phonon-polaritons in Boron Nitride for Near-field Optical Imaging and Focusing. *Nat. Commun.* **6**, 7507 doi:10.1038/ncomms8507 (2015).
6 Yoxall, E. *et al*. Direct Observation of Ultraslow Hyperbolic Polariton Propagation with Negative Phase Velocity. *Nat. Photon.* **9**, 674-678 (2015).
7 Narimanov, E. E. *et al*. Metamaterials: Naturally Hyperbolic. *Nat. Photon.* **9**, 214-216 (2015).
8 Xia, F. *et al*. Rediscovering Black Phosphorus as an Anisotropic Layered Material for Optoelectronics and Electronics. *Nat. Commun.* **5**, 4458 doi:10.1038/ncomms5458 (2014).
9 Qiao, J. *et al*. High-mobility Transport Anisotropy and Linear Dichroism in Few-layer Black Phosphorus. *Nat. Commun.* **5**, 4475 doi:10.1038/ncomms5475 (2014).
10 Yuan, H. *et al*. Polarization-sensitive Broadband Photodetector Using a Black Phosphorus Vertical p-n Junction. *Nat. Nanotech.* **10**, 707-713 (2015).
11 Tombros, N. *et al*. Anisotropic Spin Relaxation in Graphene. *Phys. Rev. Lett.* **101**, 046601 (2008).
12 Han, W. *et al*. Graphene Spintronics. *Nat. Nanotech.* **9**, 794-807 (2014).
13 Raes, B. *et al*. Determination of the Spin-lifetime Anisotropy in Graphene Using Oblique Spin Precession. *Nat. Commun.* **7**, 11444 doi:10.1038/ncomms11444 (2016).
14 Zeng, H. *et al*. Valley Polarization in MoS_2 Monolayers by Optical Pumping. *Nat. Nanotech.* **7**, 490-493 (2012).
15 Mak, K. F. *et al*. Control of Valley Polarization in Monolayer MoS_2 by Optical Helicity. *Nat. Nanotech.* **7**, 494-498 (2012).
16 Geim, A. K. *et al*. van der Waals Heterostructures. *Nature* **499**, 419-425 (2013).
17 Novoselov, K. S. *et al*. 2D Materials and van der Waals Heterostructures. *Science* **353**, 462-472 (2016).
18 Liu, Y. *et al*. van der Waals Heterostructures and Devices. *Nat. Rev. Mater.* **1**, 16042 doi:10.1038/natrevmats.2016.42 (2016).
19 Jariwala, D. *et al*. Mixed-dimensional van der Waals Heterostructures. *Nat. Mater.* **16**, 170-181 (2017).
20 Withers, F. *et al*. Light-emitting Diodes by Band-structure Engineering in van der Waals Heterostructures. *Nat. Mater.* **14**, 301-306 (2015).
21 Palacios-Berraquero, C. *et al*. Atomically Thin Quantum Light-emitting Diodes. *Nat. Commun.* **7**, 12978 doi: 10.1038/ncomms12978 (2016).
22 Woessner, A. *et al*. Highly Confined Low-loss Plasmons in Graphene – Boron Nitride Heterostructures. *Nat. Mater.* **14**, 421-425 (2014).
23 Caldwell, J. D. *et al*. van der Waals Heterostructures: Mid-infrared Nanophotonics. *Nat. Mater.* **14**, 364-366 (2015).
24 Yang, X. *et al*. Far-field Spectroscopy and Near-field Optical Imaging of Coupled Plasmon-Phonon Polaritons in 2D van der Waals Heterostructures. *Adv. Mater.* **28**, 2931-2938 (2016).
25 Massicotte, M. *et al*. Picosecond Photoresponse in van der Waals Heterostructures. *Nat. Nanotech.* **11**, 42-46 (2016).
26 Castellanos-Gomez, A. *et al*. Why All the Fuss About 2D Semiconductors. *Nat. Photon.* **10**, 202-204 (2016).
27 W, Y. L. *et al*. Optical Anisotropy in Layer Compounds. *J. Phys. C: Solid State Phys.* **6**, 551-565 (1973).
28 Weber, J. W. *et al*. Optical Constants of Graphene Measured by Spectroscopic Ellipsometry. *Appl. Phys. Lett.* **97**, 91901-91904 (2010).
29 Born, M. *et al*. *Principles of Optics*; Cambridge University Press: Cambridge, U.K., 1999.
30 Fei, Z. *et al*. Gate-tuning of Graphene Plasmons Revealed by Infrared Nano-imaging. *Nature* **487**, 82-85 (2012).
31 Chen, J. *et al*. Optical Nano-imaging of Gate-tunable Graphene Plasmons. *Nature* **487**, 77-81 (2012).
32 Dai, S. *et al*. Tunable Phonon Polaritons in Atomically Thin van der Waals Crystals of Boron Nitride.

Science **343**, 1125-1129 (2014).
33 Kang, J. *et al*. Goos-Hänchen Shift and Even – odd Peak Oscillations in Edge-reflections of Surface Polaritons in Atomically Thin Crystals. *Nano Lett.* **17**, 1768-1774 (2017).
34 Hu, F. *et al*. Imaging Exciton – Polariton Transport in $MoSe_2$ Waveguides. *Nat. Photon.* **11**, 356-360 (2017).
35 Kumar, A. *et al*. Tunable Dielectric Response of Transition Metals Dichalcogenides MX_2 (M=Mo, W; X=S, Se, Te): Effect of Quantum Confinement. *Physica B.* **407**, 4627-4634 (2012).
36 Kumar, A. *et al*. A First Principle Comparative Study of Electronic and Optical Properties of 1H – MoS_2 and 2H – MoS_2. *Mater. Chem. Phys.* **135**, 755-761 (2012).
37 Bozhevolnyi, S. I. *et al*. Near-field Characterization of Photonic Crystal Waveguides. *Semicond. Sci. Tech.* **21**, R1-R16 (2006).
38 Fei, Z. *et al*. Nano-optical Imaging of WSe_2 Waveguide Modes Revealing Light-exciton Interactions. *Phys. Rev. B* **94**, 081402 (2016).
39 Knoll, B. *et al*. Mid-infrared Scanning Near-field Optical Microscope Resolves 30 nm. *J. Microsc.* **194**, 512-515 (1999).
40 Cvitkovic, A. *et al*. Analytical Model for Quantitative Prediction of Material Contrasts in Scattering-type Near-Field Optical Microscopy. *Opt. Express* **15**, 8550-8565 (2007).
41 Gao, L. *et al*. Exploitation of Multiple Incidences Spectrometric Measurements for Thin Film Reverse Engineering. *Opt. Express* **20**, 15734-15751 (2012).
42 Hu, J. *et al*. Understanding Leaky Modes - Slab Waveguide Revisited. *Adv. Opt. Photonics* **1**, 58-106 (2009).
43 Ishii, T. *et al*. Growth of Single Crystals of Hexagonal Boron Nitride. *J. Cryst. Growth* **61**, 689-690 (1983).
44 Franke, E. *et al*. In Situ Infrared and Visible-light Ellipsometric Investigations of Boron Nitride Thin Films at Elevated Temperatures. *J. Appl. Phys.* **84**, 526-532 (1998).
45 Chenet, D. A. *et al*. In-plane Anisotropy in Mono- And Few-layer ReS_2 Probed by Raman Spectroscopy and Scanning Transmission Electron Microscopy. *Nano Lett.* **15**, 5667-5672 (2015).
46 Li, Y. *et al*. Probing Symmetry Properties of Few-layer MoS_2 and h-BN by Optical Second-harmonic Generation. *Nano Lett.* **13**, 3329-3333 (2013).

Acknowledgements

This work is supported by the National Basic Key Research Program of China (No. 2015CB932400 and 2016YFA0202000), the National Natural Science Foundation of China (No. 51372045, 11504063, and 11674073), the key program of the bureau of Frontier Sciences and Education Chinese Academy of Sciences (No. QYZDB-SSW-SLH021). Z.P.S. acknowledges funding from the Academy of Finland (No. 276376, 284548, 295777, 304666), TEKES (OPEC), and the European Union's Seventh Framework Program (No. 631610).

Author contributions

Q.D. and M.K.L. designed and supervised the research. D.B.H. deduced the equations and performed the experiments. R.N.L. prepared the samples. All the authors were involved in the data analysis and manuscript preparation.

Additional information

Supplementary Information accompanies this paper can be found at http://www.nature.com/naturecommunications.

Competing financial interests: The authors declare no competing financial interests.

Legends for Figure 1

Figure 1 | Schematics of the experimental setup and the near-field imaging principle. (**a**) Three dimensional schematic of the near-field setup. The sharp edges of MoS_2 nanoflakes are aligned to the Y axis and the s-SNOM tip scans along the X axis. Inset is the top view of the experimental setup. α is the angle between the illumination wavevector k_0 and its projection in the X-Y plane k_{xy}, β is the angle between k_{xy} and the investigated sample edges. (**b**) Front view of the experimental setup. The tip-launched waveguide modes are scattered into free space at the sample edges and interfere with the tip-scattered light at the photodetector. (**c**) Near-field images and real-space fringe profiles of the 81-nm-thick MoS_2 sample with $\beta = 60°$ and $\beta = 35°$, respectively. Λ_L is the fringe spacing at the left half of the near-field images while Λ_R is that at the right half. (**d**) Momentum-space spectra of the fringe profiles in c, the difference between the left and right side apparent wavevectors decreases with the reduction of β.

Legends for Figure 2

Figure 2 | Experimental results. (**a**) Near-field images and real-space fringe profiles of MoS_2 samples with different thicknesses. (**b**) Momentum-space spectra of fringe profiles in a. In the experiments, the MoS_2 nanoflakes are all placed in the same orientation as in Figure 1**a**. The low-frequency peaks in **b** showing no thickness dependence are the trivial air modes. Note that in b the left part of the second spectrum (d=103 nm) is multiplied by four.

Legends for Figure 3

Figure 3 | Analyses of Experimental Results. (**a**) Theoretical and experimental thickness dispersions of the fundamental ordinary (TE_0) and extraordinary (TM_0) waveguide modes in the air-MoS_2-SiO_2 three-layer waveguide, the superstrate air, and the substrate SiO_2 are assumed to be semi-infinite in the calculations. (**b**) Theoretical thickness dispersions of the fundamental ordinary (TE_0) and extraordinary (TM_0) waveguide modes in freestanding MoS_2 nanoflakes. (**c**) Evolution of mode profiles associated with the fundamental ordinary waveguide mode (TE_0), the inset shows a decreasing coupling factor between the tip-induced hot spot and the waveguide mode with increasing sample thickness. We assume the interval $0\ \text{nm} \le z \le 100\ \text{nm}$ to be the efficient coupling region since the tip tapping amplitude is set to 50 nm in the experiments. (**d**) Normalized mode profiles of the fundamental ordinary (TE_0) and extraordinary (TM_0) waveguide modes for the 170-nm-thick MoS_2 sample indicate the extraordinary mode retains stronger electric field at the virtual SiO_2/Si interface and tends to leak out through the SiO_2 layer. The calculations in **c** and **d** use the same air-MoS_2-SiO_2 three-layer waveguide model as in **a**.

Legends for Figure 4

Figure 4 | Probing optical anisotropy of h-BN in the visible region. Experimental results for (**a**) 75-nm-thick and (**b**) 230-nm-thick h-BN samples. In **a**, the h-BN nanoflake was placed in the same orientation as in Figure 1**a**; in **b**, the two opposite edges are not exactly parallel and there are small angles between the edges and the direction of the s-SNOM tip cantilever as shown in Supplementary Fig. 9**b**. There is a small frequency difference between the air modes in **a** and **b** because of the different β angles shown in Supplementary Fig. 9. Note that in **b** the spectrum taken at the right edge is multiplied by three.

Supplementary Note 1: Polarization States of Waves in Anisotropic Media

The wave equation in a homogeneous non-magnetic anisotropic medium is[1]

$$\nabla^2\mathbf{E}+k_0^2\left\|\varepsilon\right\|\mathbf{E}=\nabla\left(\nabla\cdot\mathbf{E}\right), \tag{1}$$

where $\left\|\varepsilon\right\|$ is the relative dielectric tensor. In the coordinate system aligned to the optic axis of a uniaxial anisotropic crystal, $\left\|\varepsilon\right\|$ can be expressed as

$$\left\|\varepsilon\right\|=\begin{bmatrix}\varepsilon_\perp & 0 & 0\\ 0 & \varepsilon_\perp & 0\\ 0 & 0 & \varepsilon_\parallel\end{bmatrix}, \tag{2}$$

where $\varepsilon_\perp$ is the relative dielectric constant perpendicular to the optic axis, and $\varepsilon_\parallel$ is the relative dielectric constant parallel to the optic axis.

Supplementary Equation (1) actually contains three equations, one for each dimension. Explicitly, these equations can be expressed in the matrix form as

$$\begin{bmatrix}k_y^2+k_z^2-\varepsilon_\perp k_0^2 & -k_xk_y & -k_xk_z\\ -k_yk_x & k_x^2+k_z^2-\varepsilon_\perp k_0^2 & -k_yk_z\\ -k_zk_x & -k_zk_y & k_x^2+k_y^2-\varepsilon_\parallel k_0^2\end{bmatrix}\begin{bmatrix}E_x\\ E_y\\ E_z\end{bmatrix}=0 \tag{3}$$

where $\mathbf{k}=\left(k_x,k_y,k_z\right)$ is the wavevector and $\mathbf{E}=\left(E_x,E_y,E_z\right)$ is the electric field. For a homogeneous wave in the Y direction, we have $k_y=0$, then Supplementary Equation (3) can be reduced to

$$\begin{bmatrix}k_z^2-\varepsilon_\perp k_0^2 & 0 & -k_xk_z\\ 0 & k_x^2+k_z^2-\varepsilon_\perp k_0^2 & 0\\ -k_zk_x & 0 & k_x^2-\varepsilon_\parallel k_0^2\end{bmatrix}\begin{bmatrix}E_x\\ E_y\\ E_z\end{bmatrix}=0. \tag{4}$$

For Supplementary Equation (4) to have a non-trivial solution (i.e. non-zero electric field), the determinant of the matrix must be zero:

$$\begin{vmatrix} k_z^2 - \varepsilon_\perp k_0^2 & 0 & -k_x k_z \\ 0 & k_x^2 + k_z^2 - \varepsilon_\perp k_0^2 & 0 \\ -k_z k_x & 0 & k_x^2 - \varepsilon_\parallel k_0^2 \end{vmatrix} = 0 . \quad (5)$$

Solving Supplementary Equation (5) we get two sets of solutions:

$$k_{z1} = \sqrt{\varepsilon_\perp k_0^2 - k_x^2},\ \mathbf{E}_{\mathrm{TE}} = \begin{bmatrix} 0 \\ E_y \\ 0 \end{bmatrix} \quad (6)$$

corresponding to the transverse electric (TE) polarized ordinary wave, and

$$k_{z2} = \sqrt{\frac{\varepsilon_\perp}{\varepsilon_\parallel}}\sqrt{\varepsilon_\parallel k_0^2 - k_x^2},\ \mathbf{E}_{\mathrm{TM}} = \begin{bmatrix} E_x \\ 0 \\ E_z \end{bmatrix}. \quad (7)$$

corresponding to the transverse magnetic (TM) polarized extraordinary wave.

Supplementary Note 2: Eigenequations for Anisotropic Planar Waveguide

A three layer planar waveguide composed of an isotropic semi-infinite superstrate (ε_1), an anisotropic guiding layer ($\|\varepsilon\|$) with the thickness *d*, and an isotropic semi-infinite substrate (ε_2) is shown in Supplementary Fig. 1. The optic axis of the guiding layer is parallel to the Z axis.

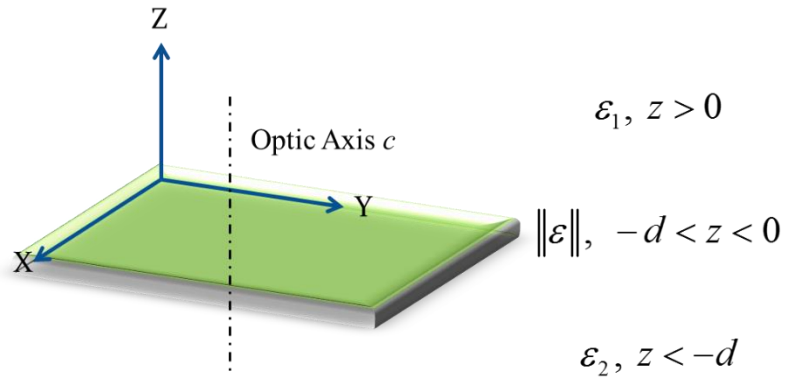

Supplementary Figure 1 | Schematic of a three-layer planar waveguide. The superstrate and substrate are both semi-infinite and optically isotropic. The optic axis of the anisotropic guiding layer is perpendicular to the basal plane.

For a waveguide mode (ordinary or extraordinary) propagating in the X direction in the three-layer planar waveguide shown in Supplementary Fig. 1, the electric field can be expressed as

$$\begin{cases} \mathbf{E}_1(\mathbf{r},t) = \mathbf{E}_1^0 e^{-\alpha_1 z} e^{i(\beta x-\omega t)} = (E_{1x}^0, E_{1y}^0, E_{1z}^0) e^{-\alpha_1 z} e^{i(\beta x-\omega t)} \\ \mathbf{E}_{\mathrm{g}}(\mathbf{r},t) = \mathbf{E}_{\mathrm{g}}^0 \cos(\alpha_{\mathrm{g}} z+\varphi) e^{i(\beta x-\omega t)} = (E_{\mathrm{g}x}^0, E_{\mathrm{g}y}^0, E_{\mathrm{g}z}^0) \cos(\alpha_{\mathrm{g}} z+\varphi) e^{i(\beta x-\omega t)} \\ \mathbf{E}_2(\mathbf{r},t) = \mathbf{E}_2^0 e^{\alpha_2 (z+d)} e^{i(\beta x-\omega t)} = (E_{2x}^0, E_{2y}^0, E_{2z}^0) e^{\alpha_2 (z+d)} e^{i(\beta x-\omega t)} \end{cases}, \tag{8}$$

where $\beta = k_x$ is the propagation constant of the waveguide mode (not to be confused with the angle in Figure 1 in the main text), $\alpha_{\mathrm{g}} = k_z$.

For the electric fields in the isotropic superstrate and substrate, Supplementary Equation (1) can be reduced to

$$\nabla^2 \mathbf{E} + k_0^2 \varepsilon_{1,2} \mathbf{E} = 0. \tag{9}$$

Substituting $\mathbf{E}_1$ and $\mathbf{E}_2$ into Supplementary Equation (9), we get

$$\begin{cases} \alpha_1^2 = \beta^2 - k_0^2 \varepsilon_1 \\ \alpha_2^2 = \beta^2 - k_0^2 \varepsilon_2 \end{cases}. \tag{10}$$

Imposing Gauss's law $\nabla \cdot \left(\varepsilon_{1,2} \mathbf{E}\right) = 0$ on $\mathbf{E}_1$ and $\mathbf{E}_2$, we get

$$\begin{cases} \mathbf{E}_1(\mathbf{r},t) = (E_{1x}^0, E_{1y}^0, \dfrac{i\beta}{\alpha_1} E_{1x}^0) e^{-\alpha_1 z} e^{i(\beta x-\omega t)} \\ \mathbf{E}_2(\mathbf{r},t) = (E_{2x}^0, E_{2y}^0, \dfrac{-i\beta}{\alpha_2} E_{2x}^0) e^{\alpha_2 (z+d)} e^{i(\beta x-\omega t)} \end{cases}. \tag{11}$$

Imposing the Gauss's law $\nabla \cdot \left(\|\varepsilon\| \mathbf{E}\right) = 0$ on $\mathbf{E}_{\mathrm{g}}$, we get

$$\mathbf{E}_{\mathrm{g}}(\mathbf{r},t) = \mathbf{E}_{\mathrm{g}}^0 \cos(\alpha_{\mathrm{g}} z+\varphi) e^{i(\beta x-\omega t)} = \left[\frac{\varepsilon_{\parallel} \alpha_{\mathrm{g}} \sin(\alpha_{\mathrm{g}} z+\varphi)}{\varepsilon_{\perp} i\beta \cos(\alpha_{\mathrm{g}} z+\varphi)} E_{\mathrm{g}z}^0, E_{\mathrm{g}y}^0, E_{\mathrm{g}z}^0 \right] \cos(\alpha_{\mathrm{g}} z+\varphi) e^{i(\beta x-\omega t)}. \tag{12}$$

Using the Faraday's law $\nabla \times \mathbf{E} = i\omega\mu_0 \mathbf{H}$, we can get magnetic fields from Supplementary Equation (11) and (12)

$$\begin{cases} \mathbf{H}_1 = \dfrac{-i}{\omega\mu_0}(\alpha_1 E_{1y}^0, \dfrac{k_0^2\varepsilon_1}{\alpha_1} E_{1x}^0, i\beta E_{1y}^0) e^{-\alpha_1 z} e^{i(\beta x-\omega t)} \\ \mathbf{H}_{\mathrm{g}} = \dfrac{-i}{\omega\mu_0}\left[\alpha_{\mathrm{g}} \sin(\alpha_{\mathrm{g}} z+\varphi) E_{\mathrm{g}y}^0, -i\beta\cos(\alpha_{\mathrm{g}} z+\varphi) E_{\mathrm{g}z}^0 - \alpha_{\mathrm{g}} \sin(\alpha_{\mathrm{g}} z+\varphi) E_{\mathrm{g}x}^0, i\beta\cos(\alpha_{\mathrm{g}} z+\varphi) E_{\mathrm{g}y}^0\right] e^{i(\beta x-\omega t)} \\ \mathbf{H}_2 = \dfrac{-i}{\omega\mu_0}(-\alpha_2 E_{2y}^0, -\dfrac{k_0^2\varepsilon_2}{\alpha_2} E_{2x}^0, i\beta E_{2y}^0) e^{\alpha_2(z+d)} e^{i(\beta x-\omega t)} \end{cases} \quad (13)$$

For a TE polarized ordinary waveguide mode, there are three field components (H_x, E_y, H_z). Imposing the interface conditions on $\mathbf{H}_x$ and $\mathbf{E}_y$ at the two interfaces ($z=0,\ z=$-d), we get

$$\begin{cases} \alpha_1 E_{1y}^0 = \alpha_{\mathrm{g}} \sin\varphi E_{\mathrm{g}y}^0 \\ \alpha_{\mathrm{g}} \sin(-\alpha_{\mathrm{g}} d+\varphi) E_{\mathrm{g}y}^0 = -\alpha_2 E_{2y}^0 \\ E_{1y}^0 = \cos\varphi E_{\mathrm{g}y}^0 \\ \cos(-\alpha_{\mathrm{g}} d+\varphi) E_{\mathrm{g}y}^0 = E_{2y}^0 \end{cases}, \quad (14)$$

which can be reformulated into

$$\alpha_{\mathrm{g}} d = \tan^{-1}\left(\frac{\alpha_1}{\alpha_{\mathrm{g}}}\right) + \tan^{-1}\left(\frac{\alpha_2}{\alpha_{\mathrm{g}}}\right) + m\pi \ (\alpha_{\mathrm{g}} = \sqrt{\varepsilon_\perp k_0^2 - \beta^2}) . \quad (15)$$

Substituting α_1 α_2 and α_{g} into Supplementary Equation (15) and let $\beta_{\mathrm{o}} = \beta$, we can get the eigenvalue equation for TE polarized ordinary waveguide modes

$$\sqrt{\varepsilon_\perp k_0^2 - \beta_{\mathrm{o}}^2}\, d = \tan^{-1}\left(\frac{\sqrt{\beta_{\mathrm{o}}^2 - k_0^2\varepsilon_1}}{\sqrt{\varepsilon_\perp k_0^2 - \beta_{\mathrm{o}}^2}}\right) + \tan^{-1}\left(\frac{\sqrt{\beta_{\mathrm{o}}^2 - k_0^2\varepsilon_2}}{\sqrt{\varepsilon_\perp k_0^2 - \beta_{\mathrm{o}}^2}}\right) + m\pi . \quad (16)$$

Similarly, for the TM polarized extraordinary waveguide mode (E_x, H_y, E_z), we have

$$\sqrt{\frac{\varepsilon_\perp}{\varepsilon_\parallel}}\sqrt{\varepsilon_\parallel k_0^2 - \beta_{\mathrm{e}}^2}\, d = \tan^{-1}\left(\frac{\sqrt{\beta_{\mathrm{e}}^2 - k_0^2\varepsilon_1}\,\varepsilon_\perp}{\sqrt{\frac{\varepsilon_\perp}{\varepsilon_\parallel}}\sqrt{\varepsilon_\parallel k_0^2 - \beta_{\mathrm{e}}^2}\,\varepsilon_1}\right) + \tan^{-1}\left(\frac{\sqrt{\beta_{\mathrm{e}}^2 - k_0^2\varepsilon_2}\,\varepsilon_\perp}{\sqrt{\frac{\varepsilon_\perp}{\varepsilon_\parallel}}\sqrt{\varepsilon_\parallel k_0^2 - \beta_{\mathrm{e}}^2}\,\varepsilon_2}\right) + n\pi , \quad (17)$$

where $\beta_{\mathrm{e}} = \beta$. In Supplementary Equation (16) and (17) m and n are non-negative integers.

Supplementary Note 3: Mode Profiles Normalization and Coupling Factors Calculation

According to Poynting's theorem, the power density in the X direction carried by the ordinary (TE) and extraordinary (TM) waveguide modes can be expressed as

$$P_{\mathrm{o}} = \frac{1}{2} E_y(z) H_z(z) = \frac{\beta_{\mathrm{o}}}{2\omega\mu_0} \int_{-\infty}^{+\infty} E_y^2(z) dz \tag{18}$$

and

$$P_{\mathrm{e}} = -\frac{1}{2} E_z(z) H_y(z) = \frac{k_0^2}{2\omega\mu_0\beta_{\mathrm{e}}} \left[\int_{-\infty}^{-d} \varepsilon_2 E_{2z}^2(z) dz + \int_{-d}^{0} \varepsilon_{\parallel} E_{\mathrm{gz}}^2(z) dz + \int_{0}^{+\infty} \varepsilon_1 E_{1z}^2(z) dz \right], \tag{19}$$

respectively. Thus, the ordinary and extraordinary mode profiles can be normalized as

$$\bar{E}_y(z) = \frac{E_y(z)}{\sqrt{P_{\mathrm{o}}}} \tag{20}$$

and

$$\bar{E}_z(z) = \frac{E_z(z)}{\sqrt{P_{\mathrm{e}}}}, \tag{21}$$

respectively. Of course, Supplementary Equation (20) and (21) can be further normalized by dividing the maximum of $\bar{E}_y(z)$ and $\bar{E}_z(z)$ — $\max\left\{\bar{E}_y(z), \bar{E}_z(z)\right\}$.

If we take the interval $0\ \mathrm{nm} \le z \le 100\ \mathrm{nm}$ to be the efficient coupling region of the waveguide modes and the s-SNOM tip-induced hot spot, the coupling factors can be defined as

$$CF_{\mathrm{o}} = \frac{\int_0^{100} \bar{E}_y(z) dz}{\int_{-\infty}^{+\infty} \bar{E}_y(z) dz} \tag{22}$$

and

$$CF_{\mathrm{e}} = \frac{\int_0^{100} \bar{E}_z(z) dz}{\int_{-\infty}^{+\infty} \bar{E}_z(z) dz} \tag{23}$$

for the ordinary and extraordinary modes, respectively.

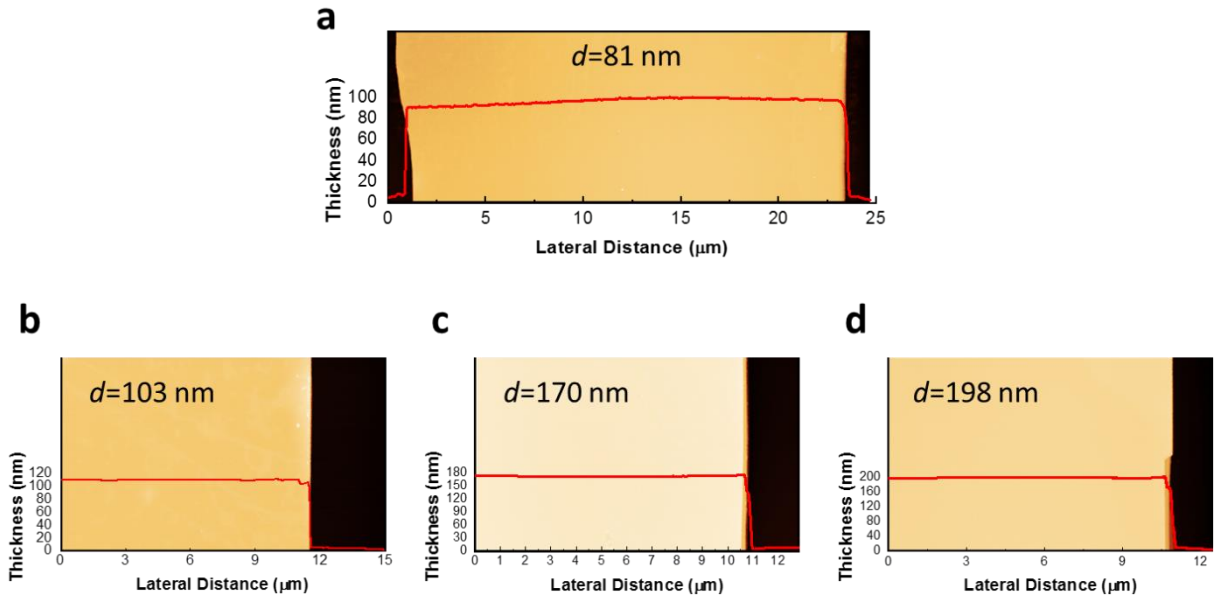

Supplementary Figure 2 | AFM images and height profiles for MoS_2 samples of different thicknesses. (**a**) *d*=81 nm; (**b**) *d*=103 nm; (**c**) *d*=170 nm; (**d**) *d*=198 nm.

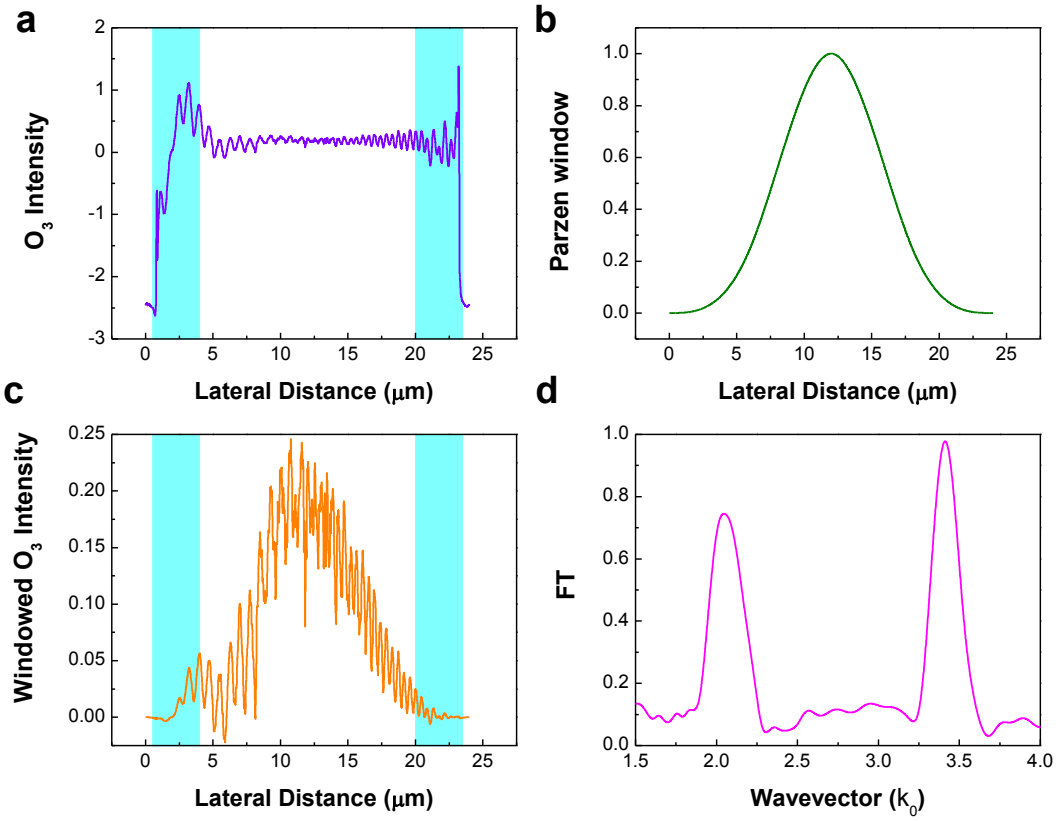

Supplementary Figure 3 | The schematic diagram of using a window function to suppress the edge effect in Fourier transform. (**a**) Subtract the average value of the whole profile from the original data to suppress the DC component in the momentum-space spectra, the shadowed areas indicate where the edge effect exists, widths of the shadows are 3 μm; (**b**) The Parzen window function used to suppress the edge effect; (**c**) The windowed optical profile obtained by multiplying **a** with **b**, the shadowed areas indicate that the edge effect has been effectively suppressed; (**d**) The Fourier transform of **c**, reflecting mainly the spatial frequencies in the center areas of the near-field images.

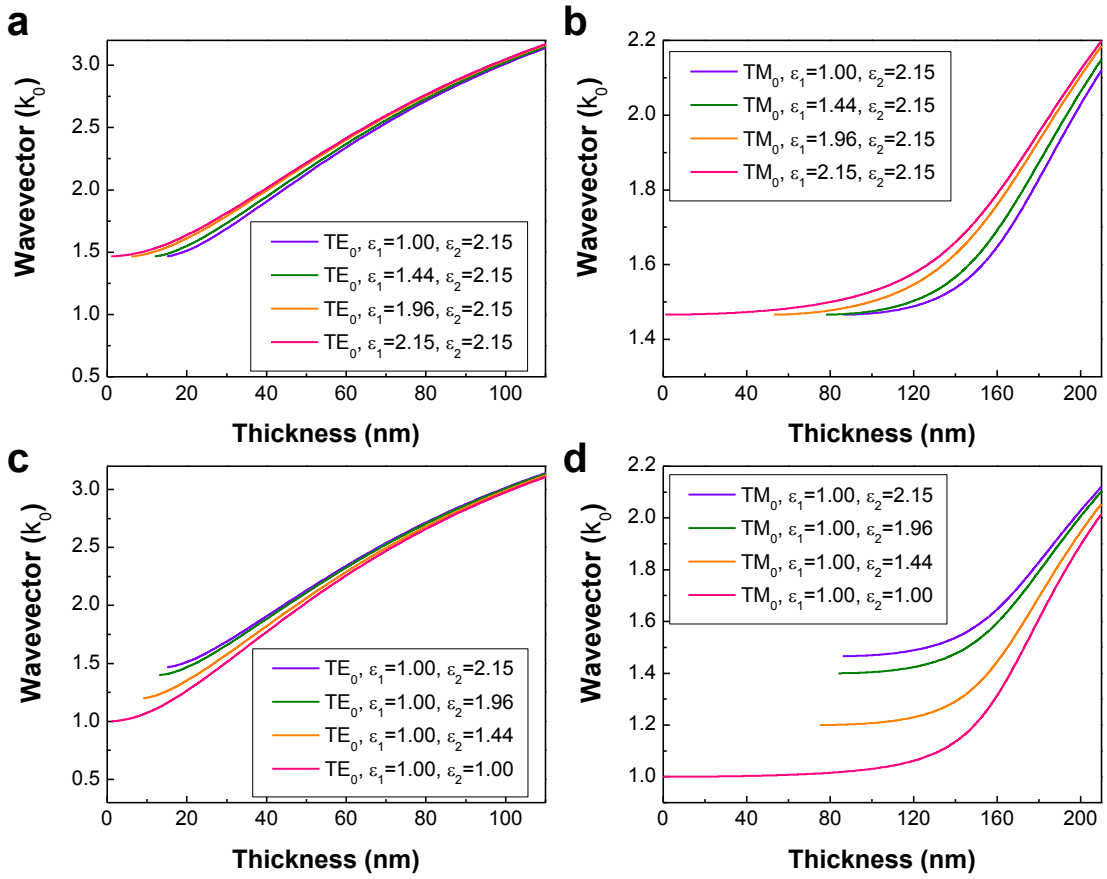

Supplementary Figure 4 | Thickness dispersions of MoS_2 waveguide with different degrees of symmetry. (**a**) and (**b**) Thickness dispersions of the TE_0 and TM_0 mode with increasing superstrate dielectric constant, respectively; (**c**) and (**d**) Thickness dispersions of the TE_0 and TM_0 mode with decreasing substrate dielectric constant, respectively. The cut-off thickness decreases with the increasing degree of symmetry.

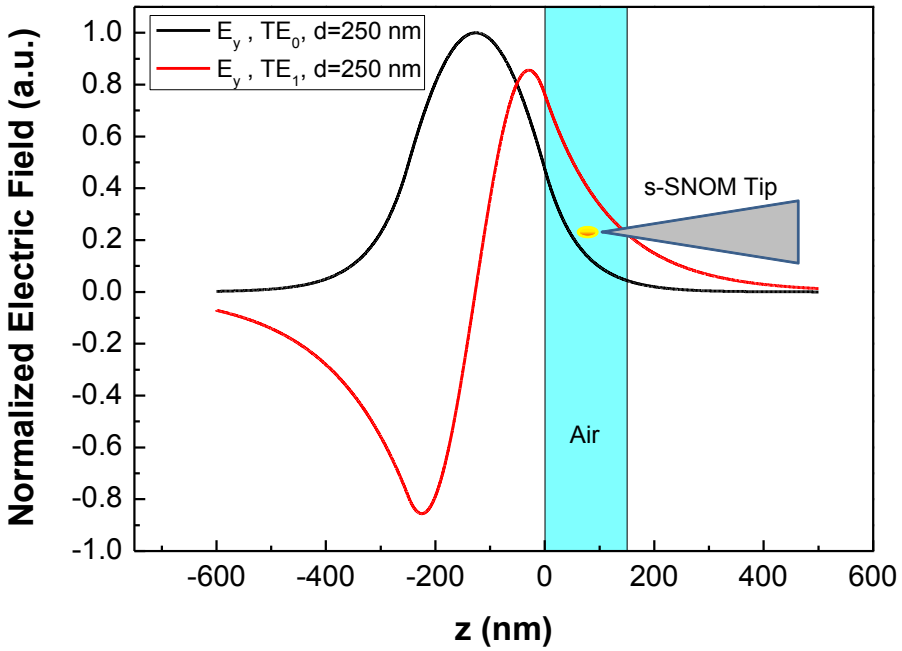

Supplementary Figure 5 | Electric field profiles of the fundamental and the first order TE waveguide modes. The high order modes possess smaller in-plane wavevectors compared with the fundamental modes, thus their evanescent fields extend much further out of the sample surface, leading to high excitation efficiencies of these high order waveguide modes and the enhanced interference visibilities in the s-SNOM images.

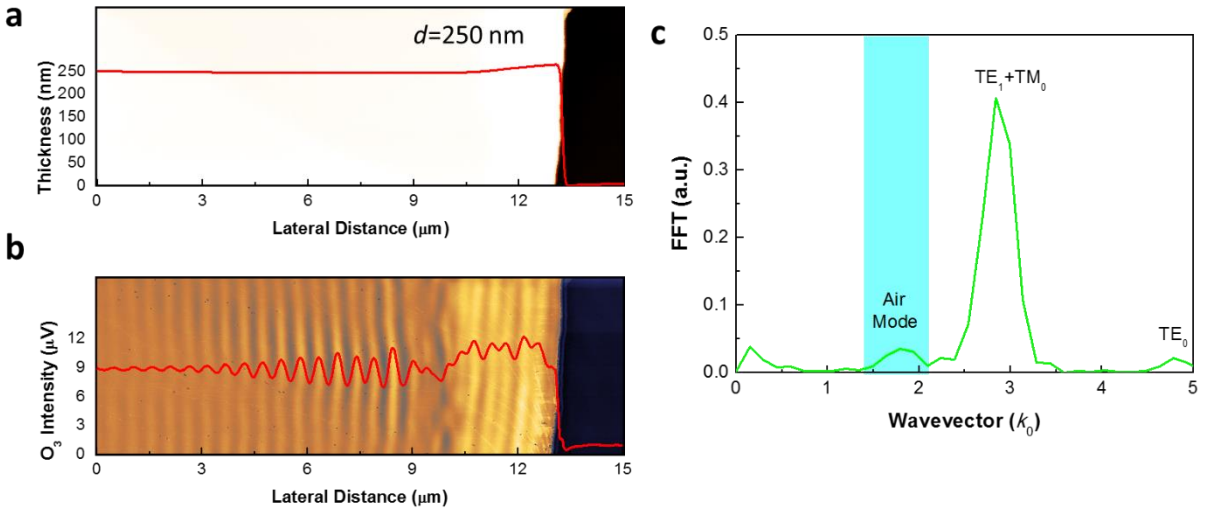

Supplementary Figure 6 | Experimental verification of enhanced interference visibility of TE$_1$ mode. We used a 250-nm-thick MoS_2 sample supporting the first order TE mode to verify our explanation of the varying interference visibilities in Supplementary Fig 5 and main text. (**a**) AFM image and height profile for a 250-nm-thick MoS_2 sample; (**b**) Near-field image and optical profile of the 250-nm-thick MoS_2 sample; (**c**) Spatial frequency domain spectrum of the optical profile in **b**. Note that the frequency difference between TE_1 and TM_0 is expected to be $0.177k_0$, too small to be resolved in **c**.

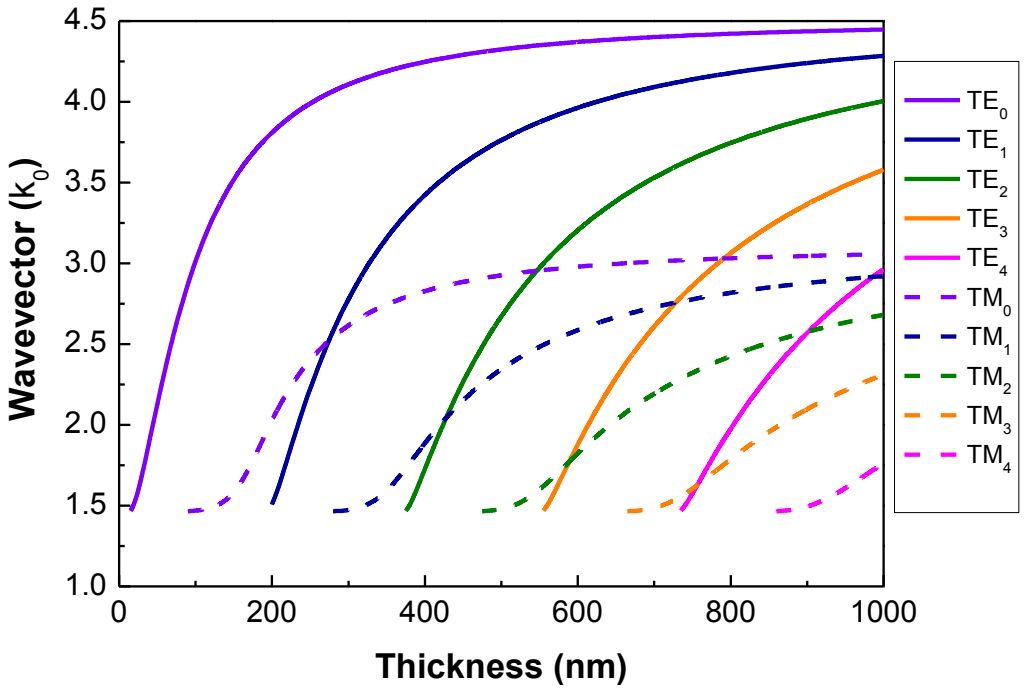

Supplementary Figure 7 | Thickness dispersions of air-MoS_2-SiO_2 waveguide. The MoS_2 thickness range from 0 to 1000 nm. There are five TE modes (m=0~4) and five TM modes (n=0~4) for a waveguide of a 1000-nm-thick MoS_2 guide layer.

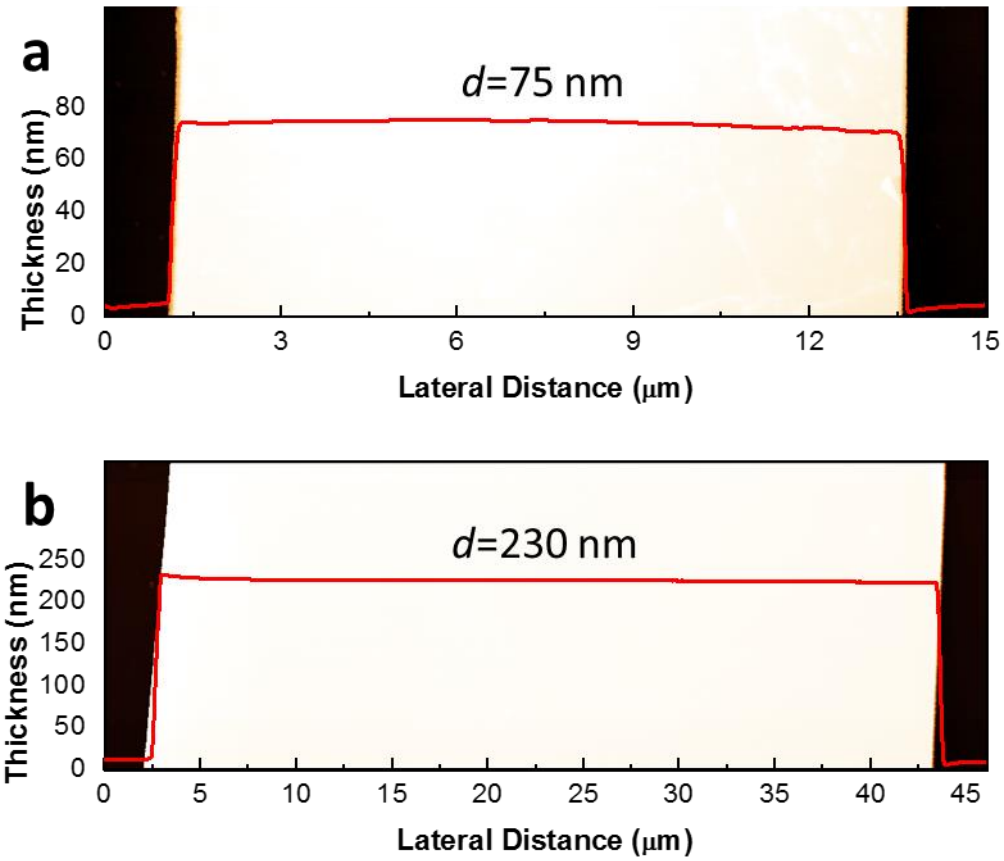

Supplementary Figure 8 | AFM images and height profiles for h-BN samples of different thicknesses. (**a**) *d*=75 nm; (**b**) *d*=230 nm.

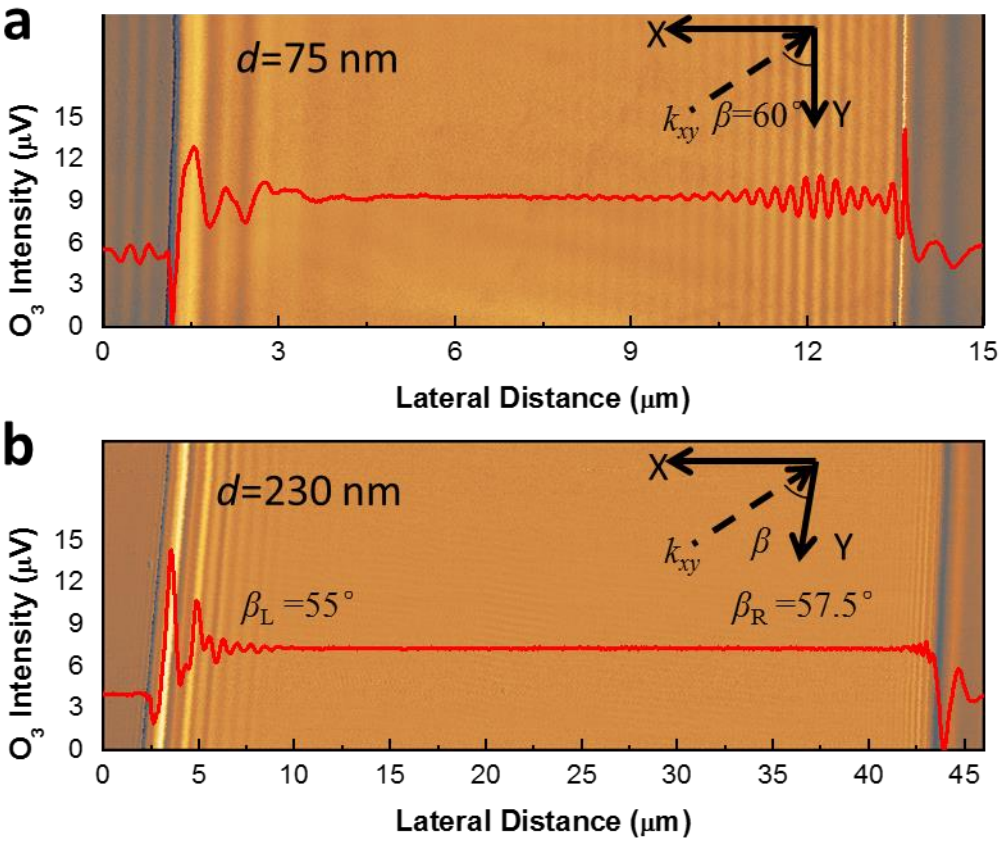

Supplementary Figure 9 | Large-area near-field images and real-space fringe profiles of h-BN samples. (**a**) *d*=75 nm; (**b**) *d*=230 nm.

Supplementary References

1 Born, M. *et al*. *Principles of Optics*; Cambridge University Press: Cambridge, U.K., 1999.